Journal of Materials Chemistry A

Unravelling the water oxidation mechanism on NaTaO3–based photocatalyst

Journal:	*Journal of Materials Chemistry A*
Manuscript ID	TA-ART-12-2019-014235.R1
Article Type:	Paper
Date Submitted by the Author:	03-Mar-2020
Complete List of Authors:	Ding, Qian; State Key Laboratory of Catalysis, Dalian Institute of Chemical Physics, Chinese Academy of Sciences Liu, Yang; Dalian Institute of Chemical Physics Chen, Tao; State Key Laboratory of Catalysis, Dalian Institute of Chemical Physics, Chinese Academy of Sciences, Dalian National Laboratory for Clean Energy, Wang, Xiaoyu; University at Buffalo, State University of New York, Department of Chemical and biological engineering and Computation and Data-enabled Science and Engineering Program Feng, Zhaochi; Dalian Institute of Chemical Physics, State Key Laboratory of Catalysis Wang, Xiuli; Dalian Institute of Chemical Physics, State Key Laboratory of Catalysis Dupuis, Michel; University at Buffalo, State University of New York, Department of Chemical and biological engineering and Computation and Data-enabled Science and Engineering Program Li, Can; Dalian Institute of Chemical Physics, State Key Laboratory of Catalysis;

Unravelling the water oxidation mechanism on $NaTaO_3$–based photocatalyst

Qian Ding[†,‡,⊥], Yang Liu[†,‡,⊥], Tao Chen[†,§], Xiaoyu Wang[//], Zhaochi Feng[†], Xiuli Wang[*,†], Michel Dupuis[*,//], Can Li[†]

[†] State Key Laboratory of Catalysis, Dalian Institute of Chemical Physics, Chinese Academy of Sciences, Dalian National Laboratory for Clean Energy, Dalian 116023, China. E-mail: xiuliwang@dicp.ac.cn

[‡] University of Chinese Academy of Sciences, Beijing 100049, China

[§] School of Marine Science and Environment Engineering, Dalian Ocean University, 52 Heishijiao Street, Dalian, 116023, China

[//] Department of Chemical and Biological Engineering, University at Buffalo, State University of New York, Buffalo 14260, USA. E-mail: mdupuis2@buffalo.edu

[⊥] These two authors equally contributed to the work.

Abstract

Understanding the detailed kinetics and mechanisms of water oxidation is crucial because water oxidation is the bottleneck reaction in overall water splitting. Here, we investigated the photocatalytic water oxidation on $NaTaO_3$-based photocatalysts. With *in situ* FT-IR spectroscopy, two new water oxidation intermediates with IR absorption peaks centered at 1058 and 935 cm^{-1} were observed and assigned to Ta(VI)=O and Ta(O_2) peroxo species, respectively. With $H_2{}^{18}O$ as reactant and $NaTa^{16}O_3$ as photocatalyst, both $^{16}O^{18}O$ and $^{18}O_2$ were evolved continuously from overall water splitting as analyzed by mass spectroscopy (MS), demonstrating that the lattice O atoms in $NaTaO_3$-based photocatalysts participate in the formation of O_2 during the reaction. DFT results are consistent with formation of Ta=O, $^{16}O^{18}O$ and $^{18}O^{18}O$ intermediates and products, while predicting that several water oxidation pathways are thermodynamically accessible for water oxidation on $NaTaO_3$. Based on these observations, we propose a three-step two-site mechanism for photocatalytic water oxidation on $NaTaO_3$-based photocatalysts in which lattice oxygens play a key role. The elucidation of the present mechanism should help in understanding broadly water oxidation on semiconductor-based photocatalysts.

Key words: Water oxidation, $NaTaO_3$, photocatalysis, *in situ* FT-IR spectroscopy, DFT calculation, lattice oxygen

1. Introduction

Photocatalytic overall water splitting on metal oxide surface has attracted much attention because it is one of the most desirable approaches for utilizing the solar energy.[1-3] Water oxidation is the bottleneck reaction in overall water splitting.[4-7] Identification of water oxidation intermediates and investigation of the kinetics of these intermediates are crucial for understanding the water oxidation mechanisms.

To date, mechanistic studies of water oxidation have mainly focused on homogeneous water oxidation catalysts. Two fundamental water oxidation mechanisms, the acid-base mechanism and the direct coupling mechanism, have been invoked for homogeneous water oxidation catalysts.[8] The two mechanisms differ primarily with respect to the number of sites involved in the reaction, especially in the O-O bond formation step: one active site is involved in the acid-base mechanism in contrast to two active sites in the direct coupling mechanism, respectively. In either of these water oxidation mechanisms, the active sites are metal ion sites.[8]

Much research has been devoted to establishing the mechanism(s) of water oxidation on heterogeneous catalysts. Significant insight has arisen by identifying the reaction intermediates. For heterogeneous TiO_2 photocatalyst, surface TiOOH and TiOOTi peroxo intermediates[9] were detected during photocatalytic water oxidation in the presence of Fe^{3+} ions acting as electron scavenger.[10] For Co_3O_4 nanoparticles, an oxo Co(IV) site and a surface superoxide were observed.[11] For hematite photoanodes, both an Fe^{IV}=O intermediate[12] and a superoxide species[13] were reported also. Recently, a Ti-$O^{\cdot}$ oxyl radical was shown to be a nascent catalytic intermediate of water oxidation

at a *n*-$SrTiO_3$/aqueous interface.[14] All these intermediates are associated with the metal ion sites, demonstrating that these sites play an essential role also in heterogeneous water oxidation. Thus for both homogeneous and heterogeneous water oxidation catalysts, the metal ions are regarded as the active sites for water oxidation.

A few computational studies of heterogeneous water oxidation mechanisms have suggested that lattice oxygen atoms are involved in the reaction of water oxidation on perovskite electrocatalysts.[15, 16] Using in situ ^{18}O isotope-labelling mass spectrometry, Yang Shao-Horn *et al.* demonstrated that O_2 generated during water oxidation come from lattice oxygen for strongly covalent metal oxides.[17] The participation of lattice oxygens in water oxidation mechanisms is fundamentally different from the schemes based on metal sites as active sites. More detailed investigations are needed to understand how lattice oxygens participate in the reaction and what the reaction intermediates are.

Perovskite $NaTaO_3$ doped with lanthanum and loaded with NiO has been found to exhibit high quantum yield (~ 56%) for overall water splitting.[18] However, the nature of the water oxidation reaction intermediates and the reaction mechanism in overall water splitting on $NaTaO_3$-based photocatalysts are still unclear. This finding points to the possibility and benefits of studying the overall water splitting process on this material without sacrificial agents. We report here such an investigation. We use the perovskite structure of sodium tantalate $NaTaO_3$ to study whether and how lattice oxygens are involved in water oxidation. We performed in situ FT-IR transmission spectroscopy and in situ mass spectroscopy with $H_2{}^{18}O$ and D_2O to detect and identify

intermediates. Based on experimental observations we formulate a three-step two-site mechanism that has not been formulated to date and that is supported by density functional theory (DFT) computation for water oxidation. The paper is organized as follows: in Section 2, we give the experimental details. In Section 3, we provide the computational details. In Section 4, we describe and discuss the experimental findings, first from *in situ* FT-IR spectroscopy, then from *operando* mass spectrometry. We then present the computational results and analyze various possible mechanisms. We summarize and conclude in Section 5.

2. Experimental details

The $NaTaO_3$ and $NaTaO_3$:La catalysts were prepared by the solid-state reaction method.[18] The starting materials, La_2O_3, Na_2CO_3, Ta_2O_5 were mixed according to the ratio Na:La:Ta=0.98:0.02:1 supposing that the sodium ions were replaced by lanthanum ions. An excess amount of sodium (5 mol %) was added in the mixture to compensate for volatilization. The mixture was calcined in air at 1170 K for 1 hour and 1420 K for 10 hours. The NiO/$NaTaO_3$:La catalyst with NiO loading of 0.2 wt % was prepared by the impregnation method. $NaTaO_3$:La was dispersed into a $Ni(NO_3)_3$ aqueous solution and stirred overnight. After evaporation at 363 K, the dry power was calcined in air at 540 K for 1 hour.

In situ IR absorption spectra were recorded on a Nicolet 470 FT-IR spectrometer equipped with a MCT (HgCdTe) detector. The sample (~ 40 mg) was pressed into a self-supporting wafer and purged with N_2, then water vapor (2.4877 kPa) was introduced into the IR cell by the bubble method. The light source was a 266 nm laser

(Quanta-Ray INDI Nd:YAG Laser) with pulse duration of 6-8 ns (20 Hz, 70 mW), when the spectra were scanned 64 times.

Isotopic labelled water splitting experiments detected by a mass spectroscopy were performed in a He flow reactor. 40 mg $NaTaO_3$ sample was immersed in 0.5 mL water ($H_2{}^{18}O$, 90% atom% ^{18}O). The reactor was flowed with He after the immersion of the photocatalysts in $H_2{}^{18}O$, then it was irradiated for 25 min with a 263 nm laser (UVISIR, 1 kHz) with the laser power of 200 mW. The evolved H_2 and O_2 were analyzed with a mass spectrometer (GAM200, InProcess Instruments). The mass/charge ratio (m/z) values, 2, 32, 34 and 36, were analyzed for H_2, $^{16}O_2$, $^{16}O^{18}O$, and $^{18}O_2$, respectively.

FT-IR spectrum of H_2O_2 was recorded by dipping 30% H_2O_2 aqueous solution on the crystal in AIR-IR cell. For FT-IR spectra of the H_2O_2 adsorption on the $NaTaO_3$-based photocatalysts, a drop of 30% H_2O_2 aqueous solution was adhered on the catalyst wafer when the FT-IR spectra recorded after the adsorbed H_2O_2 was blown away by N_2 were used as FT-IR background.

3. Computational details

We studied the water oxidation mechanism with DFT computation using the Vienna Ab-initio Simulation Package (VASP)[19, 20]. Spin-polarized calculations were performed with PBE[21] functional using a GGA+U method[22] with U_{eff} = 2.0 eV for Ta atoms[23]. The projector-augmented wave (PAW) potentials[24, 25] were used to represent the core-valence electron interactions with valence electrons described with plane waves with an energy cutoff of 400 eV. The valence electrons for Na, Ta, O and H were ($2p^6 3s^1$), ($5p^6 5d^3 6s^2$), ($2s^2 2p^4$), and ($1s^1$), respectively. Gaussian smearing with a 0.05

eV width aided the electronic wavefunction convergence. As often done in the literature, we modeled the reaction mechanism at a solid/vacuum interface[26-28]. We analyzed the mechanism on the basis of the thermodynamic stability of the intermediates.

We first calculated surface energies for various low-index surfaces. In accord with previous studies of $NaTaO_3$[18, 29], the {001} and {110} surfaces were found to be the most stable surfaces of orthorhombic $NaTaO_3$ (Table S1). Therefore, we focused on these surfaces for our investigation. We created 5-layer slab models with ~16 Å vacuum spaces from a fully optimized orthorhombic $NaTaO_3$ unit cell (illustrated in Figure S1 and Figure S2). In both cases Ta and O atoms are exposed at the terminating surface and Na atoms are in a sub-surface layer. A 9×9×6 Monkhorst-Pack k-mesh grid was used for k-point sampling of the unit cell in bulk calculations, while 2×2×1 and 2×1×1 Monkhorst-Pack k-mesh grids were used in the optimizations of all (001) slabs and (110) slabs, respectively. During the geometry optimizations and energy calculations, the bottom two layers of the slabs were fixed at their bulk positions while the top three layers of the slabs, including the adsorbates, were fully relaxed until the forces on all atoms were less than 0.005 eV/Å. In a recent paper, Ouhbi and Aschauer[30] modeled water oxidation on $NaTaO_3$ (001) surface and proposed free energy diagram and mechanism based on a 4-1 model (4 layers - 1 frozen layer). The data shown in Table S2, Figure S3 and S4 suggest that the 4-1 model may not be converged. We adopted a 5-2 model (5 layers - 2 frozen layers). A dipole correction was applied throughout the calculations to offset the charge polarization effects in the asymmetric stoichiometric slabs[31].

The water oxidation free energy changes at pH = 7, pressure p = 1 bar, T = 298.15 K were derived using the principles of material and energy balance:

$\Delta G = \Delta E + \Delta ZPE - T\Delta S$, with $\Delta E = E_{products} - E_{reactors}$,

and ΔE is the reaction energy calculated by DFT. The differences in zero-point energies, ΔZPE, and the change in entropy ΔS were derived from the reference publication listed in Table S3. The temperature dependence of the enthalpy was neglected in the calculations, i.e., ΔH (298 K→0 K) = 0. Using the standard hydrogen electrode (SHE) as a reference, the free energy for a proton and an electron $G(H^+) + G(e^-)$ were replaced by ½ $G(H_2)$. The effect of pH on $G(H^+)$ was corrected for the proton concentration dependence of the free energy $\Delta G_{pH} = (- \ln 10) \times kT \times pH$. The free energies presented and discussed below all include the pH correction of $\Delta G_{pH} \sim -0.414$ eV for pH=7. For reaction steps involving the formation of O_2, the free energy for O_2 was taken as the experimental reaction free energy $\Delta G(O_2) = 4.92$ eV + $2G(H_2O) - 2G(H_2)$ for water splitting, because DFT (GGA+U) does not describe the electronic structure of the O_2 molecule accurately enough.

4. Results and Discussion

4.1 Identification of water oxidation intermediates with *in situ* FT-IR spectroscopy

The structure characterizations of $NaTaO_3$ samples demonstrate that the photocatalysts are in perovskite structure with high crystallinity (Figure S5 and S6). NiO/$NaTaO_3$:La exhibits extremely high activity for photocatalytic overall water splitting in aqueous solution (Table S4). Moreover, it displays obvious photocatalytic water splitting activity with water vapor, which indicates that it makes sense to

investigate the water oxidation mechanism with water vapor and *in situ* FTIR transmission spectroscopy (Table S5).

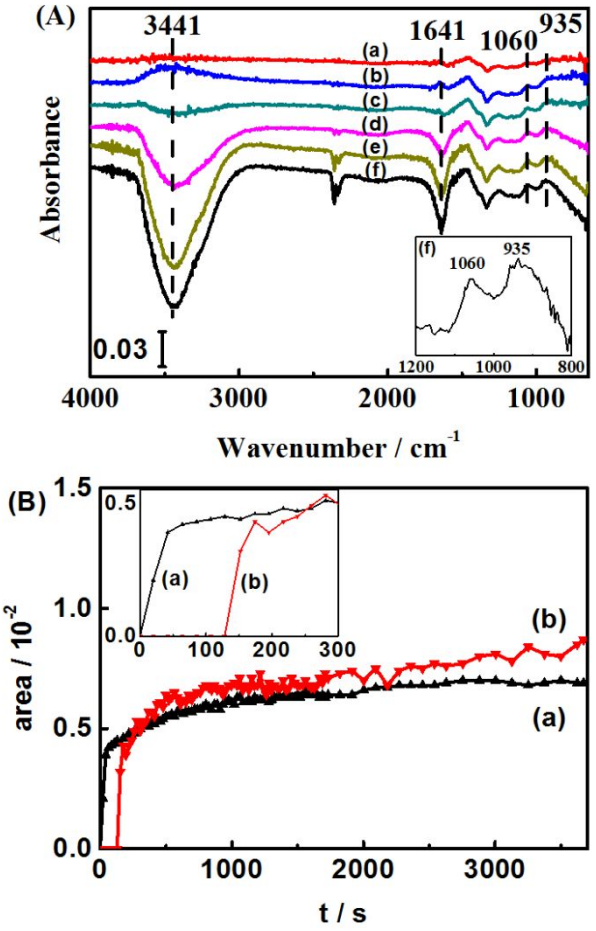

Figure 1. (A) Difference FT-IR spectra of H_2O adsorbed on 0.2 wt% $NiO/NaTaO_3$:La (2 mol%) irradiated by 266 nm laser (20 Hz, 70 mW) for (a) 20 s, (b) 85 s, (c) 175 s, (d) 300 s, (e) 1800 s, and (f) (inset) 3600 s; (B) Time-dependent relative areas of the two bands at (a) 1060 cm^{-1} and (b) 935 cm^{-1}. The time resolution used was ~20 s.

Figure 1 shows the difference FTIR spectra of a $NiO/NaTaO_3$:La wafer exposed to water vapor irradiated by 266 nm laser (20 Hz, 70 mW), with a reference spectrum taken before the irradiation as the background. The intensities of a broad band centered at 3441 cm^{-1}, a relatively sharp band at 1641 cm^{-1}, and a broad band below 900 cm^{-1} decrease with the UV irradiation time. These bands correspond to the OH stretching,

the HOH bending, and the vibrational modes of adsorbed H_2O, respectively, as demonstrated in Figure S7.[32] The decline of these bands is due to irradiation-induced water desorption and consumption of the adsorbed water molecules in the water splitting reaction. In the range of 900-1100 cm^{-1} where the vibrational bands of water oxidation intermediates are most likely to appear, two IR bands centered at 1060 cm^{-1} and 935 cm^{-1} are observed to grow with UV irradiation time (Figure 1A). These two IR bands are not observed for pure $NaTaO_3$ or $NaTaO_3$:La photocatalysts under 266 nm irradiation, nor for NiO/$NaTaO_3$:La irradiated with 532 nm laser (photon energy of ~ 2.3 eV, smaller than the ~ 4.0 eV bandgap of $NaTaO_3$) (Figure S8). These results indicate that the IR bands originate from the UV-light induced photocatalysis, not from thermally driven processes. Moreover, the intensities of 1060 and 935 cm^{-1} bands are much lower in NiO/$NaTaO_3$ than in NiO/$NaTaO_3$:La (2 mol%), although the loading amounts are the same in the two samples, demonstrating that the two IR bands are not associated with the species on NiO. The correlation of these two IR bands with the photocatalytic activities of the $NaTaO_3$ indicates that these two IR bands are likely to arise from the surface intermediates from photocatalytic water splitting. The origin of the bands appearing in the range 1250-1500 cm^{-1} is unclear at present. They might correlate with some impurities introduced during the NiO loading process because these bands were not detected under UV irradiation for the $NaTaO_3$ or $NaTaO_3$: La photocatalysts (Figure S8a and S8b).

The time evolutions of the two bands at 1060 cm^{-1} and 935 cm^{-1} were analyzed as shown in Figure 1B. The 1060 cm^{-1} band appears immediately after the UV light

irradiation, but interestingly, the appearance of the 935 cm^{-1} band shows a clear delay from the start time of the UV irradiation. The difference in time delay indicates that the bands at 1060 cm^{-1} and 935 cm^{-1} correspond to different surface intermediates. The time delay of the 935 cm^{-1} band becomes shorter with an increase in the excitation power. It remains at about 50 seconds with the excitation power above 50 mW (Figure S9). These results can be rationalized if we assume that the first intermediate species giving the 1060 cm^{-1} band is the precursor of the second intermediate species that gives the 935 cm^{-1} band. The formation and appearance of the second species can only start when the concentration of the first (parent) species grows to exceed a threshold amount. Increasing the excitation power accelerates the rate of formation of the parent species so that the second intermediates begins to appear at an earlier time.

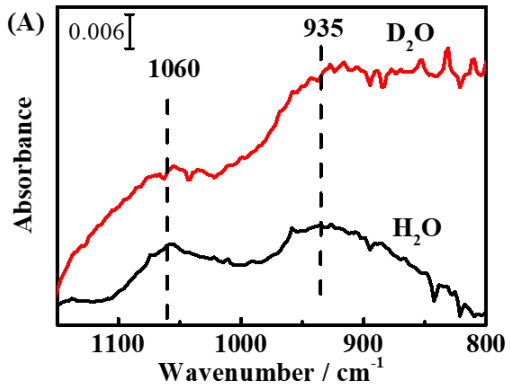

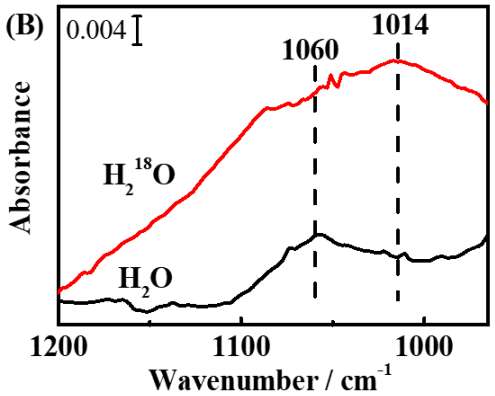

Figure 2. (A) Difference FT-IR spectra of D_2O (D>99.9%) and H_2O adsorbed on 0.2 wt% NiO/$NaTaO_3$:La (2 mol%) after UV irradiation. (B) Difference FT-IR spectra of $H_2{}^{18}O$ (90% atom% ^{18}O) (magnified fivefold) and H_2O adsorbed on 0.2 wt% NiO/$NaTaO_3$:La (2 mol%) after UV irradiation.

Next, we carried isotope-labelling FT-IR experiments by using D_2O or $H_2{}^{18}O$ water as reactants to help identify further the structure and nature of the intermediate species detected above. The results are shown in Figure 2. Comparison of the IR spectrum with D_2O vapor to that with H_2O points to the fact that no isotopic shifts are observed for both the 1060 and 935 cm^{-1} bands. A broad negative band below 900 cm^{-1} corresponding to the vibrational modes of adsorbed H_2O disappears when using D_2O as the reactant, presumably because of an isotopic shift down to a lower wavenumber range with a low signal to noise ratio. This finding indicates that both bands (at 1060 and 935 cm^{-1}) arise from species without H atoms. When $H_2{}^{18}O$ was used as the reactant, we observed the appearance of a new band at 1014 cm^{-1}, while the band at around 935 cm^{-1} disappeared, presumably shifted down into a lower wavenumber ranges with a low signal to noise ratio. These spectral changes demonstrate the contribution of oxygen to the intermediate species.

The bands at 1060 and 935 cm^{-1} that do not involve H atoms are likely associated with water oxidation on $NaTaO_3$, since NiO loaded on the photocatalyst is active as a cocatalyst for H_2 formation.[18] The vibrational band at 1060 cm^{-1} lies in the range reported for the stretching modes of metal=O species (900-1100 cm^{-1}),[33-35] or superoxide O_2^- species (1000-1200 cm^{-1}).[36-40] The assignment of the 1060 cm^{-1} band to a superoxide species can be ruled out, because it would be a three-electron intermediate

that is only one oxidation step before O_2 evolution and it is unlikely to appear in advance of the 935 cm^{-1} band. Therefore, it is reasonable to assign the 1060 cm^{-1} band to a Ta(VI)=O species, a one-electron oxidation intermediate. This assignment is supported by the isotope-labelling experiments. The observed $^{16}O/^{18}O$ isotopic shift of ~ 46 cm^{-1} is comparable with the isotopic shift of ~ 40 cm^{-1} reported for M=O species.[41, 42] Additionally, no D/H isotopic shift is observed. Lastly, we will show below that our DFT-calculated reaction energy diagram is consistent with this assignment.

The vibrational band at 935 cm^{-1} lies in the range for O-O stretching vibrations of surface peroxide species $M(O_2)$[43, 44] and it can be reasonably assigned to a $Ta(O_2)$ peroxo species. To confirm this hypothesis, FT-IR spectra of H_2O_2 adsorbed on $NaTaO_3$-based photocatalysts were obtained and the results are shown in Figure 3. The spectra show that both undissociated adsorbate H_2O_2 and dissociated adsorbate are formed on the catalyst surface. The spectra exhibit the characteristic frequencies of O-O stretching at 872 cm^{-1} for undissociated H_2O_2 and 945 cm^{-1} for dissociated adsorbate.[10, 45-48] Compared to the band at 945 cm^{-1} for a dissociated adsorbate resulting from H_2O_2 adsorption, the 935 cm^{-1} band formed during the water splitting reaction shifts only slightly. This observation supports the assignment of this band to the $Ta(O_2)$ species. This assignment is further confirmed by the isotopic-labelling experiment with deuterium as the 935 cm^{-1} band exhibits no D/H isotopic shift. The band at 1114 cm^{-1} that is observed on $NiO/NaTaO_3$ but not on $NaTaO_3$ or $NaTaO_3$:La is tentatively assigned to the bending mode for Ni-O-O-H species.

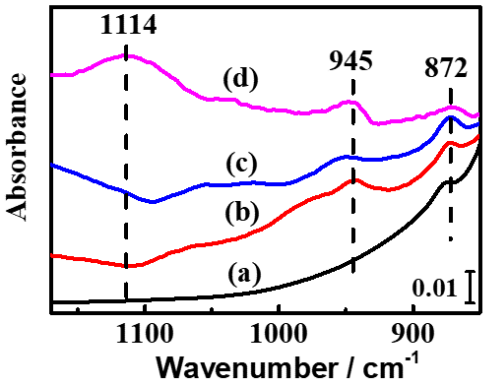

Figure 3. FT-IR spectra of H_2O_2 (a, magnified fivefold) and H_2O_2 adsorbed on $NaTaO_3$ (b), $NaTaO_3$:La (2 mol%) (c) and 0.2 wt% NiO/$NaTaO_3$ (d, magnified fivefold).

4.2 Characterization of produced O_2 by *operando* mass spectroscopy

To investigate the role of lattice oxygen in the water oxidation mechanism on $NaTaO_3$-based photocatalysts, we analyzed molecular O_2 evolved during photocatalytic $H_2{}^{18}O$ splitting by mass spectroscopy (Figure 4). Mass peaks for both $^{16}O^{18}O$ and $^{18}O_2$ were detected continuously for 25 minutes in one cycle, while no $^{16}O^{16}O$ mass was detected. These results indicate that $*^{18}OH$ dangling species and lattice ^{16}O atoms in $NaTaO_3$–based photocatalysts are involved in O_2 evolution, while coupling of two lattice O atoms can be ruled out. The amount of evolved mixed-isotope $^{16}O^{18}O$ is slightly larger than that of $^{18}O_2$. This result suggests that water oxidation has a preference to go through the lattice-oxygen mechanism over direct coupling of O's from two water molecules. This observation is also supported by the calculations below.

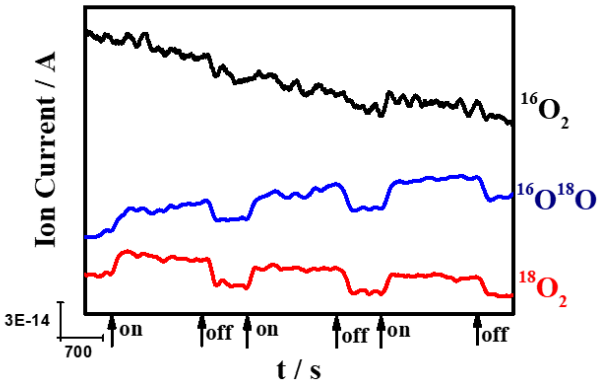

Figure 4. Mass spectroscopy from isotopic water ($H_2{}^{18}O$) splitting reaction product on 0.2 wt% NiO/$NaTaO_3$:La (2 mol%) with ^{16}O irradiated by 263 nm laser (200 mW) for 2-4 cycles.

4.3 Structures and energies of water oxidation intermediates of $NaTaO_3$ from DFT calculations

In the present case of photocatalytic water splitting on 0.2 wt% NiO/$NaTaO_3$:La (2 mol%), the NiO loaded on the photocatalyst acts as a cocatalyst for H_2 formation, and water oxidation reaction occurs on $NaTaO_3$ surface. Since water oxidation takes place on $NaTaO_3$ surfaces, it makes sense to study the mechanism with $NaTaO_3$ slab models.

We determined the structures and energies of possible intermediates of water oxidation on $NaTaO_3$ on both (001) and (110) surfaces at pH = 7. We included all structures and energy data in Figure S10, Table S6, and Table S7. The reaction free energy profile is shown in Figure 5 for the (001) surface. The free energy profile on the (110) surface is very similar and included in the SI (Figure S11). Note that in Figure 5, we do not show the water molecules, protons, and electrons involved in the elementary

reaction steps for sake of clarity. We maintained the appropriate mass balance when calculating the energy profile. Care must be taken to spell out the reaction steps associated with the various intermediates. For example, the step seen as "$*O_d \rightarrow *OOH_d$" is actually "$*O_d + H_2O \rightarrow *OOH_d + (H^+ + e^-)$". We considered the intermediate species $*H_2O$, *OH, *O (dangling and surface oxo), and *OOH (dangling and 'surface' species) that are often discussed in the literature[11, 27, 49-52].

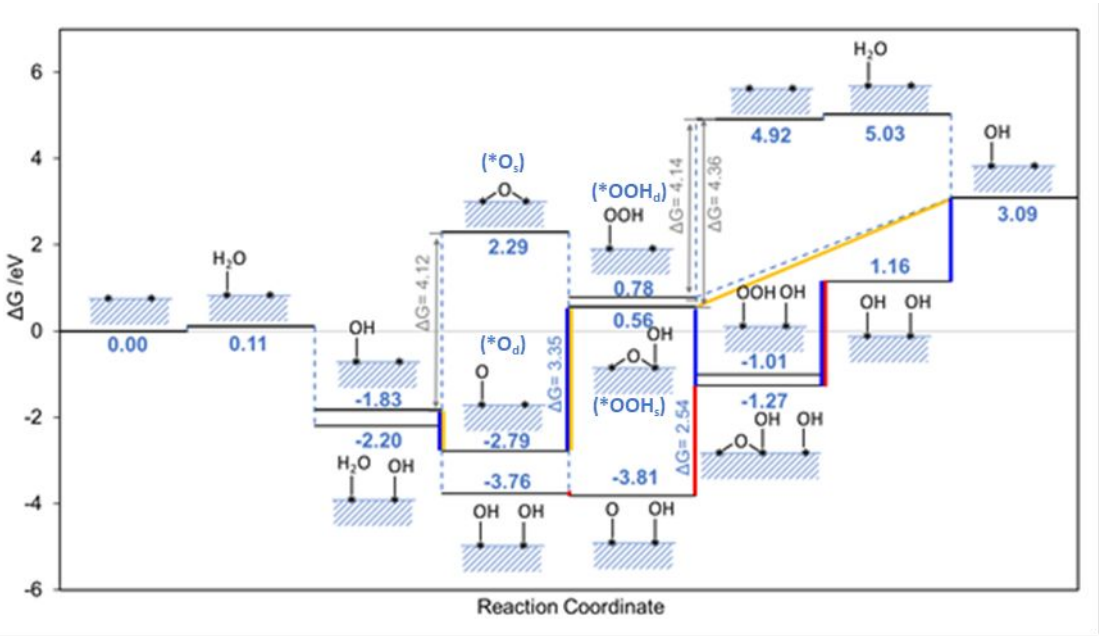

Figure 5. Free energy profile for water oxidation on (001) surface at pH = 7. Schematic structures of intermediates and step free energies are included. Water molecules H_2O, protons, and electrons that participate in the reaction steps are omitted for clarity, e.g. the "$*O_d \rightarrow *OOH_d$" step is in fact "$*O_d + H_2O \rightarrow *OOH_d + (H^+ + e^-)$". Mass balance was maintained in all elementary steps. Three pathways of interest are indicated with connecting dotted lines in red, yellow and blue. The yellow pathway referred as ***M1*** in the text starts from *OH (at ~ -1.83 eV) to form $*O_d$ (at ΔG ~ -2.79 eV), followed by $*OOH_s$ (at ΔG ~ +0.56 eV), and returning to *OH (at ΔG ~ +3.09 eV) after O_2 evolution.

Species like *O and *OOH can adopt two different structures, a 'dangling' structure and a 'surface oxo' structure.[26] It can be seen in Figure 5 that the 'dangling O' structure (denoted $*O_d$) is by far the most stable form of *O in comparison with the

'surface oxo' structure (denoted $*O_s$) where the O atom inserts into a Ta-O bond to form a Ta-O-O-Ta chemical motif. The *OOH intermediate prefers a structure that combines a 'surface oxo' adjacent to a hydroxyl species (the combined structure is denoted $*OOH_s$) in comparison to a 'dangling' *OOH (denoted $*OOH_d$). This finding holds for both the (001) and (110) surfaces (see Table S6). It is reasonable to attribute the features observed in the *in situ* FT-IR spectrum assigned as signals from Ta(VI)=O and $Ta(O_2)$ to the most stable forms of *O and *OOH, namely $*O_d$ and $*OOH_s$.

We used Figure 5 to consider the reaction pathways with $\Delta G < 4$ eV since UV-light with energy above ~ +4.0 eV can induce the h^+/e^- pair generation for $NaTaO_3$.[18, 29, 53] We note again that the adsorption of H_2O on 5-fold coordinated Ta sites is weak (~ +0.11 eV) while the adsorption of *OH is very strong (~ -1.83 eV).

We describe now the most facile mechanism, ***M1*** (highlighted in yellow in Figure 5):

Mechanism M1:

1. $*OH \rightarrow *O_d + (H^+ + e^-)$
2. $*O_d + H_2O \rightarrow *OOH + (H^+ + e^-)$
3. $*OOH + H_2O \rightarrow *OH + O_2 + 2\,(H^+ + e^-)$

$*OOH_s$ is the more stable form of *OOH and requires the least energy for the O-O coupling $*O_d \rightarrow *OOH$ step. However, a pathway going through the less stable form, OOH_d, is also accessible. In any case, the catalytic cycle can be formulated as starting from *OH, forming $*O_d$, then $*OOH_s$ or OOH_d, and lastly, evolving O_2 while returning to the starting state as *OH. Along the $*OOH_s$ pathway, the rate-determining step is

step ***2*** that requires a step free energy of ~ +3.35 eV (one-electron step), while step ***3*** requires +2.53 eV as a two-electron step. Along the $*OOH_d$ pathway, the rate-determining step is also step ***2***, with step ***3*** requiring ~ +2.31 eV.

The above results indicate that adsorption of *OH on $NaTaO_3$ is strongly thermodynamically favored. As calculated in Table S8, $NaTaO_3$ has an adsorption energy ΔE_{*OH} ~ -1.81 eV. Such large exothermic *OH adsorption is rare but has been previously reported for $LaTiO_3$ (ΔE_{*OH} = -1.55 eV).[28] In the present case of $NaTaO_3$, the calculated DFT binding energy of $*OOH_s$ is ΔE_{*OOHs} = -1.38 eV (see Table S8). The adsorption energy difference $E_{*OOH} - E_{*OH}$ is ~ 3.2 eV, in good accord with the universal scaling relationship $E_{*OOH} - E_{*OH} \approx 3.2$ eV on metal or metal oxide surface.[28, 54] This observation gives credence to our DFT results.

The strong binding energy of *OH to the surface led us to consider whether neighboring *OH species might come into play in the reaction. To this end we considered the same intermediates as before but with *OH species absorbed on nearest Ta sites. We refer to these as 'neighboring *OH' species. The energy diagram of Figure 5 indicates that intermediates that include neighboring *OH's are also low energy intermediates. We think it is unlikely that O-O coupling could involve three or more reactive sites, suggesting that additional *OH groups would be spectators.

As shown in Figure 5, in all cases except for $*O_d$, a neighboring *OH species increases the exothermic step energy by an amount essentially equal to the step energy of an isolated *OH. The effects are nearly additive: ~ -1.93 eV between *OH and *OH + *OH, ~ -1.79 eV between $*OOH_d$ and $*OOH_d$ + *OH, ~ -1.83 eV between $*OOH_s$

and *OOH_s + *OH, and ~ -1.73 eV between *O_s and *O_s + *OH, to be compared to the *OH step energy of ~ -1.83 eV. The notable exception is *O_d with a smaller increase in exothermic step energy of only ~ -1.02 eV between *O_d and *O_d + *OH. Neighboring OH's stabilize different intermediates by different amount, thus altering the free energy steps along the water oxidation pathways. In the presence of a neighboring *OH adsorbed on a nearby Ta site, the *O_d and *OOH_s species are still the preferred forms for *O and *OOH respectively, just like they were without the neighboring *OH, as *OOH can adopt both forms, *OOH_s and *OOH_d. With 'neighboring *OH' species, two other water oxidation pathways are possible. Perhaps the most significant observation is that they have smaller free energy steps even though the fundamental structural features of the intermediates remain unchanged. A modified mechanism labeled ***M2*** is as follows:

Mechanism M2:

1. $*OH + *OH \rightarrow *O_d + *OH + (H^+ + e^-)$
2. $*O_d + *OH + H_2O \rightarrow *OOH + *OH + (H^+ + e^-)$
3. $*OOH + *OH + H_2O \rightarrow *OH + *OH + O_2 + 2\,(H^+ + e^-)$

The ***M2*** mechanism (red in Figure 5) is similar to ***M1*** above, except that neighboring *OH's are involved. As seen in Figure 5, ***M2*** has step ***2*** as rate-determining step, with a step free energy of ~ +2.54 eV (to form *OOH_s). With a neighboring *OH next to *OOH_s, the reaction can proceed via mechanism ***M3*** (blue in Figure 5) as follows:

Mechanism M3:

1. $*OH \rightarrow *O_d + (H^+ + e^-)$

2. $*O_d + H_2O \rightarrow *OOH + (H^+ + e^-)$
3. $*OOH + H_2O \rightarrow *OOH + *OH + (H^+ + e^-)$
4. $*OOH + *OH + H_2O \rightarrow *OH + *OH + O_2 + 2\,(H^+ + e^-)$
5. $*OH + *OH + (H^+ + e^-) \rightarrow *OH + H_2O$

Mechanism ***M3*** has the same first two steps as ***M1.*** Step ***2*** is also the rate-determining step in ***M3*** with a step free energy of ~ +3.35 eV.

In summary, when neighboring *OH species are accounted for in the water oxidation process, the free energy step of the rate-determining step in ***M2*** is reduced from ~ +3.35 eV to ~ +2.54 eV, indicating that a neighboring *OH appears to make the water oxidation pathway more facile. However, as already pointed out, ***M2*** or ***M3*** do not bring different structural features for the reaction intermediates. Accordingly, the ***M1*** mechanism is a good overall representation of the water oxidation reaction on $NaTaO_3$.

It is of interest to compare the three-step ***M1*** mechanism to the traditional four-step coupled proton-electron mechanism,[26, 46, 55] which can be written as $* \rightarrow *OH \rightarrow *O \rightarrow *OOH \rightarrow * + O_2$. As depicted in Figure 5 for the (001) surface, the $* \rightarrow *OH$ step is exothermic by ~ -1.83 eV. The $*OH \rightarrow *O_d$ step is exothermic by ~ -0.96 eV, the $*O_d \rightarrow *OOH$ step is endothermic by ~ +3.35 eV to form $*OOH_s$ and by ~ +3.57 eV to form $*OOH_d$. The $*OOH_s \rightarrow *$ step is endothermic by ~ +4.36 eV and the $*OOH_d \rightarrow *$ step is endothermic by ~ +4.14 eV. Thus, the traditional four-step water oxidation mechanism is essentially forbidden by energetics, and we believe that water oxidation proceeds via the ***M1*** mechanism proposed here or its 'neighboring *OH'

variants, whereby O_2 evolves via a catalytic cycle that has *OH as the initial state. As a last point, let us remember that the present discussion is in the context of water oxidation on orthorhombic $NaTaO_3$ in neutral pH conditions. A similar pathway analysis holds for the (110) surface (see Figure S11). The mechanism can be presented pictorially as in Figure 6, with assignment of the intermediates based on experiment and supported by computation.

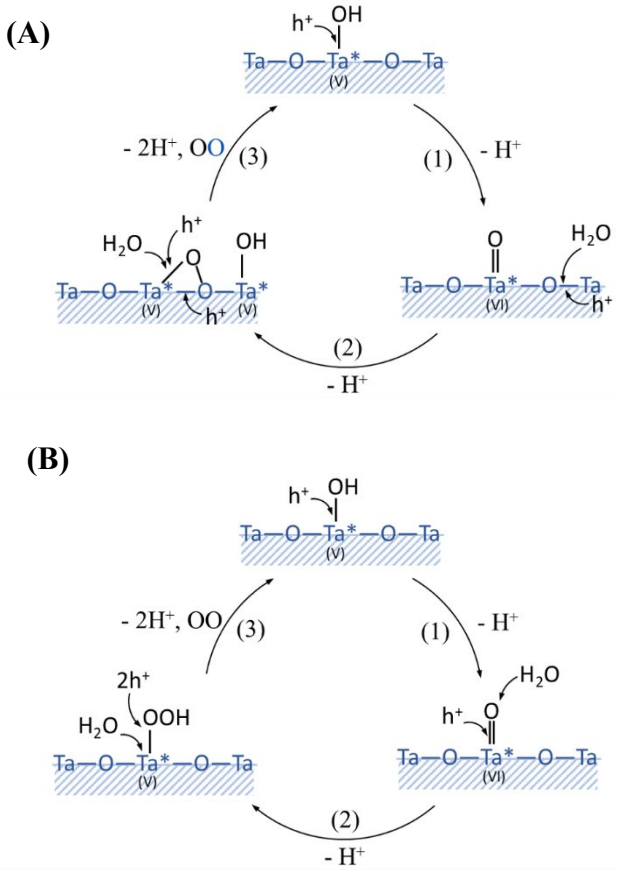

Figure 6. Proposed reaction mechanism for photocatalytic water splitting reaction on $NaTaO_3$-based catalysts: (A) formation of $^{16}O^{18}O$; (B) formation of $^{18}O^{18}O$ following the three-step ***M1*** mechanism. The lattice oxygens (^{16}O) from $NaTa^{16}O_3$ are marked in blue, while the water oxygens (^{18}O) from $H_2{}^{18}O$ are marked in black.

Figure 6A gives a 'chemical' illustration of the steps leading to the formation of

$^{16}O^{18}O$ as a part of the ***M1*** three-step mechanism. The oxidation reaction starts with the formation of a surface hydroxyl *OH species that is subsequently oxidized by a hole to form the $*O_d$ intermediate assigned earlier to a Ta(VI)=O_W species, where O_W denotes the oxygen atom originating from the oxidized water molecule. Another water molecule attacks the tantalum-oxygen bonds of the surface, Ta-O_L (where O_L represents a lattice oxygen) next to the Ta(VI)=O_W species (right hand-side scheme in Figure 6A). A hole leads to the formation of the surface Ta(O_2) moiety of the $*OOH_s$ species, a relatively stable entity with a closed-shell electronic structure (left hand-side scheme of Figure 6A). Finally, the Ta(O_2) species gets oxidized by two holes and a water molecule to release O_2 where one of the two oxygen atoms originate from the oxidized water molecule and the other oxygen atom from a surface oxygen. Upon O_2 evolution, the starting catalytic sites are recovered. With this sequence of steps, $^{16}O^{18}O$ can be produced from the photocatalytic $H_2{}^{18}O$ splitting on $NaTa^{16}O_3$. The observed long-time evolution of $^{16}O^{18}O$ suggests that lattice oxygens in the $NaTaO_3$ bulk phase diffuse to the surface to replenish the vacancy from the departed oxygen molecule.

Figure 6B shows a 'chemical' illustration of the steps leading to the formation of $^{18}O^{18}O$ as a water oxidation product. Following the same first step of ***M1*** as before, the $*O_d$ intermediate assigned to Ta(VI)=O_W is attacked by a water molecule and a hole simultaneously to form the $*OOH_d$ intermediate that had the chemical structure TaOOH (right hand-side scheme of Figure 6B). Subsequently, the TaOOH species gets oxidized by two holes and a water molecule to release O_2 (left hand-side scheme of Figure 6B), a step after which the original catalytic sites are recovered. With this mechanism, the

oxygen of $^{18}O^{18}O$ is produced from two $H_2{}^{18}O$ molecules. Similar illustrations of the $^{16}O^{18}O$ and $^{18}O^{18}O$ products via the ***M2*** and ***M3*** mechanisms are shown in Figure S12.

All three mechanisms derived from DFT calculations are consistent with the isotope experiments. As observed in the MS results (Figure 4), both $^{16}O^{18}O$ and $^{18}O_2$ are detected continuously during $H_2{}^{18}O$ water oxidation, whereby the ratio $^{16}O^{18}O$ / $^{18}O_2$ does not change much over 75-125 min. If $^{18}O_2$ are all produced following the same mechanism as $^{16}O^{18}O$ (Figure 6A) after the first cycle (one lattice ^{16}O replaced by one ^{18}O from water oxygen), the yield of $^{18}O_2$ should be extremely low at the beginning, and show an obvious increase over time as surface ^{16}O's get replaced by ^{18}O's. This is not consistent by our mass spectroscopy data of Figure 4, so the $^{18}O_2$ and $^{16}O^{18}O$ are produced following different mechanism. What's more, the amount of $^{16}O^{18}O$ product is slightly larger than that of $^{18}O_2$. Indeed, in the water oxidation mechanisms, the *OOH intermediate that is the upstream product of O_2, prefers the 'surface oxo' $*OOH_s$ form rather than the $*OOH_d$ form. The $*OOH_s$ intermediate is a structure combining a 'surface oxo' and a hydroxyl group, and the O_2 molecule originating from $*OOH_s$ will have an O atom coming from $NaTaO_3$ and the other oxygen atom from the oxidized H_2O molecule. In contrast an O_2 product formed via the $*OOH_d$ intermediate has two oxygen atoms originating from water molecules H_2O.

The participation of lattice oxygen atoms in water oxidation mechanisms is widely observed with water oxidation electrocatalysts, such as IrO_2,[56] and RuO_2.[57] The role of lattice oxygens in water oxidation mechanisms was first discussed in the context of $La_{1-x}Sr_xBO_3$ (B = transition metal) as electrocatalysts.[15] Yang Shao-Horn *et al.*

provided pieces of evidence for the participation of lattice oxygen in water oxidation processes.[17] These studies revealed that the covalency of metal-oxygen bonds is the key descriptor of what can trigger lattice-oxygen participation in oxidation. Namely, water oxidation occurs through lattice oxygen mechanisms for highly covalent oxides such as $La_{0.5}Sr_{0.5}CoO_{3-\delta}$ and $SrCoO_{3-\delta}$, but nor for the less covalent $LaCoO_3$. For $NaTaO_3$ studied in this work, prior calculations indicated that the interaction between Ta and O has a high degree of covalent character.[58, 59] The covalency of Ta-O is consistent with the lattice-oxygen oxidation mechanism on $NaTaO_3$, leading to our proposal of the ***M1*** oxidation mechanism that can lead to the formation of mixed isotope $^{16}O^{18}O$ oxygen molecule. It should be mentioned that the lattice oxygen mechanism on $NaTaO_3$ starts from a dangling oxygen $*O_d$ instead of $*O_s$, which is supposed to be the start reaction in lattice oxygen mechanism reported.[16,17,51] This is because the direct formation of $*O_s$ is inaccessible due to the large formation energy of +4.12 eV.

The water oxidation mechanism of $NaTaO_3$ determined here illustrates that the lattice oxygen atoms can play a crucial role in water oxidation over photocatalysts, just as they do in electrocatalysts. We note that $NaTaO_3$ and the other electrocatalysts on which water oxidation occurs through lattice oxygen mechanisms, are mainly of perovskite structure. Perovskite photocatalysts are a very important family of photocatalysts.[60] Over 540 kinds of perovskite materials have been studied in phtocatalysis.[61] It is possible that the three-step mechanism may occur widely in photocatalysis. For example, for the oxychloride perovskite Bi_4NbO_8Cl, the introduction of niobium Nb makes the valence band maximum predominantly

composed of O *2p* orbitals instead of Cl *3p* orbitals, resulting in water oxidation under visible light irradiation. The intrinsic reason for this activity under visible light may be the participation of oxygen lattice. The present work suggests that manipulation of valence band structure of perovskite photocatalysts may be a promising strategy for the design of highly efficient photocatalysts. Moreover, the participation of lattice oxygen atoms in the oxidation mechanism suggests that the anion atoms can be an active design factor toward efficient water oxidation.

5. **Conclusions**

In this work, the mechanism of water oxidation on $NaTaO_3$ was investigated with *in situ* FT-IR spectroscopy and *operando* mass spectroscopy, as well as DFT calculations. A new three-step mechanism in which the reaction proceeds through *OH, $*O_d$, and $*OOH_s$ was proposed. In this mechanism, lattice oxygen atoms are involved in the O_2 formation. The intermediates of Ta(VI)=O ($*O_d$) and Ta(O_2) peroxo species ($*OOH_s$) were directly observed with *in situ* FT-IR spectroscopy. The participation of lattice oxygen in the water oxidation was detected from mixed-isotope $^{16}O^{18}O$ evolution when ^{18}O isotope-labelled $H_2{}^{18}O$ served as a reactant, illustrating the crucial role of the anion atoms in photocatalytic water oxidation processes. We believe this work deepens the understanding of photocatalytic overall water splitting on metal oxide semiconductor based photocatalysts.

Acknowledgements

We acknowledge financial support from the National Natural Science Foundation of China (No. 21633015, 21872143 and 21761142018), and from the 973 National

Basic Research Program of the Ministry of Science and Technology of China (No. 2014CB239400), and from the Guidance program of Natural Science Foundation of Liaoning Province (No. 201602097). The calculations were carried out on the computer facility supported by DICP's Innovation Foundation (Grant No. DICP SZ201801). MD acknowledges also partial support from the University at Buffalo from Start-up funds.

References

1. Ruttinger, W.; Dismukes, G. C., Synthetic Water-Oxidation Catalysts for Artificial Photosynthetic Water Oxidation. *Chem. Rev.* **1997**, *97*, 1-24.
2. Barber, J., Photosynthetic Energy Conversion: Natural and Artificial. *Chem. Soc. Rev.* **2009**, *38*, 185-196.
3. Nocera, D. G., The Artificial Leaf. *Acc. Chem. Res.* **2012**, *45*, 767-776.
4. Zou, Z. G.; Ye, J. H.; Sayama, K.; Arakawa, H., Direct Splitting of Water under Visible Light Irradiation with an Oxide Semiconductor Photocatalyst. *Nature* **2001**, *414*, 625-627.
5. Young, K. J.; Martini, L. A.; Milot, R. L.; Snoeberger, R. C.; Batista, V. S.; Schmuttenmaer, C. A.; Crabtree, R. H.; Brudvig, G. W., Light-Driven Water Oxidation for Solar Fuels. *Coord. Chem. Rev.* **2012**, *256*, 2503-2520.
6. Kanan, M. W.; Nocera, D. G., *In situ* Formation of an Oxygen-Evolving Catalyst in Neutral Water Containing Phosphate and Co^{2+}. *Science* **2008**, *321*, 1072-1075.
7. Karkas, M. D.; Verho, O.; Johnston, E. V.; Akermark, B., Artificial Photosynthesis: Molecular Systems for Catalytic Water Oxidation. *Chem. Rev.* **2014**, *114*, 11863-12001.
8. Sala, X.; Maji, S.; Bofill, R.; Garcia-Anton, J.; Escriche, L.; Llobet, A., Molecular Water Oxidation Mechanisms Followed by Transition Metals: State of the Art. *Acc. Chem. Res.* **2014**, *47*, 504-516.
9. Li, Y.-F.; Liu, Z.-P.; Liu, L.; Gao, W., Mechanism and Activity of Photocatalytic Oxygen Evolution on Titania Anatase in Aqueous Surroundings. *J. Am. Chem. Soc.* **2010**, *132*, 13008-13015.
10. Nakamura, R.; Nakato, Y., Primary Intermediates of Oxygen Photoevolution Reaction on TiO_2 (Rutile) Particles, Revealed by *in situ* FTIR Absorption and Photoluminescence Measurements. *J. Am. Chem. Soc.* **2004**, *126*, 1290-1298.
11. Zhang, M.; de Respinis, M.; Frei, H., Time-Resolved Observations of Water Oxidation Intermediates on a Cobalt Oxide Nanoparticle Catalyst. *Nat. Chem.* **2014**, *6*, 362-367.
12. Zandi, O.; Hamann, T. W., Determination of Photoelectrochemical Water Oxidation Intermediates on Haematite Electrode Surfaces Using Operando Infrared Spectroscopy. *Nat. Chem.* **2016**, *8*, 778-783.

13. Zhang, Y.; Zhang, H.; Liu, A.; Chen, C.; Song, W.; Zhao, J., Rate-Limiting O-O Bond Formation Pathways for Water Oxidation on Hematite Photoanode. *J. Am. Chem. Soc.* **2018**, *140*, 3264-3269.
14. Herlihy, D. M.; Waegele, M. M.; Chen, X. H.; Pemmaraju, C. D.; Prendergast, D.; Cuk, T., Detecting the Oxyl Radical of Photocatalytic Water Oxidation at an n-$SrTiO_3$/Aqueous Interface through its Subsurface Vibration. *Nat. Chem.* **2016**, *8*, 549-555.
15. Mefford, J. T.; Rong, X.; Abakumov, A. M.; Hardin, W. G.; Dai, S.; Kolpak, A. M.; Johnston, K. P.; Stevenson, K. J., Water Electrolysis on $La_{1-x}Sr_xCoO_{3-\delta}$ Perovskite Electrocatalysts. *Nat. Commun.* **2016**, *7*, 11053.
16. Rong, X.; Parolin, J.; Kolpak, A. M., A Fundamental Relationship between Reaction Mechanism and Stability in Metal Oxide Catalysts for Oxygen Evolution. *ACS Catal.* **2016**, *6*, 1153-1158.
17. Grimaud, A.; Diaz-Morales, O.; Han, B.; Hong, W. T.; Lee, Y. L.; Giordano, L.; Stoerzinger, K. A.; Koper, M. T. M.; Shao-Horn, Y., Activating Lattice Oxygen Redox Reactions in Metal Oxides to Catalyse Oxygen Evolution. *Nat. Chem.* **2017**, *9*, 457-465.
18. Kato, H.; Asakura, K.; Kudo, A., Highly Efficient Water Splitting into H_2 and O_2 over Lanthanum-Doped $NaTaO_3$ Photocatalysts with High Crystallinity and Surface Nanostructure. *J. Am. Chem. Soc.* **2003**, *125*, 3082-3089.
19. Kresse, G.; Furthmuller, J., Efficient Iterative Schemes for Ab Initio Total-Energy Calculations Using a Plane-Wave Basis Set. *Phys. Rev. B* **1996**, *54*, 11169-11186.
20. Kresse, G.; Hafner, J., Ab Initio Molecular Dynamics for Liquid Metals. *Phys. Rev. B* **1993**, *47*, 558-561.
21. Perdew, J. P. B., K.; Ernzerhof, M., Generalized Gradient Approximation Made Simple. *Phys. Rev. Lett.* **1996**, *77*, 3865-3868.
22. Wang, L.; Maxisch, T.; Ceder, G., Oxidation Energies of Transition Metal Oxides within the GGA+U Framework. *Phys. Rev. B* **2006**, *73*, 195107.
23. Setyawan, W.; Gaume, R. M.; Lam, S.; Feigelson, R. S.; Curtarolo, S., High-Throughput Combinatorial Database of Electronic Band Structures for Inorganic Scintillator Materials. *ACS Comb. Sci.* **2011**, *13*, 382-390.
24. Kresse, G.; Joubert, D., From Ultrasoft Pseudopotentials to the Projector Augmented-Wave Method. *Phys. Rev. B* **1999**, *59*, 1758-1775.
25. Blochl, P. E., Projector Augmented-Wave Method. *Phys. Rev. B* **1994**, *50*, 17953-17979.
26. Valdes, A.; Qu, Z. W.; Kroes, G. J.; Rossmeisl, J.; Nørskov, J. K., Oxidation and Photo-Oxidation of Water on TiO_2 Surface. *J. Phys. Chem. C* **2008**, *112*, 9872-9879.
27. Seitz, L. C.; Dickens, C. F.; Nishio, K.; Hikita, Y.; Montoya, J.; Doyle, A.; Kirk, C.; Vojvodic, A.; Hwang, H. Y.; Nørskov, J. K.; Jaramillo, T. F., A Highly Active and Stable $IrO_x/SrIrO_3$ Catalyst for the Oxygen Evolution Reaction. *Science* **2016**, *353*, 1011-1014.
28. Man, I. C.; Su, H.-Y.; Calle-Vallejo, F.; Hansen, H. A.; Martínez, J. I.; Inoglu, N. G.; Kitchin, J.; Jaramillo, T. F.; Nørskov, J. K.; Rossmeisl, J., Universality in Oxygen

Evolution Electrocatalysis on Oxide Surfaces. *Chemcatchem* **2011**, *3*, 1159-1165.

29. Kudo, A.; Kato, H., Effect of Lanthanide-Doping into $NaTaO_3$ Photocatalysts for Efficient Water Splitting. *Chem. Phys. Lett.* **2000**, *331*, 373-377.

30. Ouhbi, H.; Aschauer, U., Water Oxidation Catalysis on Reconstructed $NaTaO_3$ (001) Surfaces. *J. Mater. Chem. A* **2019**, *7*, 16770-16776.

31. Bengtsson, L., Dipole Correction for Surface Supercell Calculations. *Phys. Rev. B* **1999**, *59*, 12301-12304.

32. Connor, P. A.; Dobson, K. D.; McQuillan, A. J., Infrared Spectroscopy of the TiO_2/Aqueous Solution Interface. *Langmuir* **1999**, *15*, 2402-2408.

33. Sullivan, D. H.; Harold, M. P.; Conner, W. C., Catalyst Transformation During NO+NH_3 Reaction over Vanadium Oxide Using *in situ* FTIR Emission Spectroscopy. *J. Catal.* **1998**, *178*, 108-118.

34. Kera, Y.; Hirota, K., Infrared Spectroscopic Study of Oxygen Species in Vanadium Pentoxide with Reference to Its Activity in Catalytic Oxidation. *J. Phys. Chem.* **1969**, *73*, 3973-3981.

35. Barraclough, C. G.; Lewis, J.; Nyholm, R. S., The Stretching Frequencies of Metal-Oxygen Double Bonds. *J. Chem. Soc.* **1959**, 3552-3555.

36. Zecchina, A.; Spoto, G.; Coluccia, S., Surface Dioxygen Adducts on MgO-CoO Solid-Solutions: Analogy with Cobalt-Based Homogeneous Oxygen Carriers. *J. Mol. Catal.* **1982**, *14*, 351-355.

37. Shibahara, T.; Mori, M., Raman and Infrared-Spectra of μ-O_2 Dicobalt(III) Complexes. *Bull. Chem. Soc. Jpn.* **1978**, *51*, 1374-1379.

38. Urban, M. W.; Nonaka, Y.; Nakamoto, K., Infrared and Resonance Raman Spectra of Molecular Oxygen Adducts of [N,N'-Ethylenebis(Acetylacetoniminato)]Cobalt(II). *Inorg. Chem.* **1982**, *21*, 1046-1049.

39. Nour, E. M.; Hester, R. E., Resonance Raman Studies of Oxygen Binding in Cobalt(III) Salen Complexes. *J. Mol. Struct.* **1980**, *62*, 77-79.

40. Barraclough, C. G.; Lawrance, G. A.; Lay, P. A., Characterization of Binuclear μ-Peroxo and μ-Superoxo Cobalt(III) Amine Complexes from Raman-Spectroscopy. *Inorg. Chem.* **1978**, *17*, 3317-3322.

41. Proshlyakov, D. A.; Henshaw, T. F.; Monterosso, G. R.; Ryle, M. J.; Hausinger, R. P., Direct Detection of Oxygen Intermediates in the Non-Heme Fe Enzyme Taurine/α-Ketoglutarate Dioxygenase. *J. Am. Chem. Soc.* **2004**, *126*, 1022-1023.

42. Yamada, H.; Hurst, J. K., Resonance Raman, Optical Spectroscopic, and EPR Characterization of the Higher Oxidation States of the Water Oxidation Catalyst, *cis, cis*-$[(bpy)_2Ru(OH_2)]_2O^{4+}$. *J. Am. Chem. Soc.* **2000**, *122*, 5303-5311.

43. Nakamura, R.; Imanishi, A.; Murakoshi, K.; Nakato, Y., In Situ FTIR Studies of Primary Intermediates of Photocatalytic Reactions on Nanocrystalline TiO_2 Films in Contact with Aqueous Solutions. *J. Am. Chem. Soc.* **2003**, *125*, 7443-7450.

44. Mattioli, G.; Filippone, F.; Bonapasta, A. A., Reaction Intermediates in the Photoreduction of Oxygen Molecules at the (101) TiO_2 (Anatase) Surface. *J. Am. Chem. Soc.* **2006**, *128*, 13772-13780.

45. Tozzola, G.; Mantegazza, M. A.; Ranghino, G.; Petrini, G.; Bordiga, S.; Ricchiardi, G.; Lamberti, C.; Zulian, R.; Zecchina, A., On the Structure of the Active Site of Ti-Silicalite in Reactions with Hydrogen Peroxide: A Vibrational and Computational Study. *J. Catal.* **1998**, *179*, 64-71.
46. Lin, W.; Frei, H., Photochemical and FT-IR Probing of the Active Site of Hydrogen Peroxide in Ti Silicalite Sieve. *J. Am. Chem. Soc.* **2002**, *124*, 9292-9298.
47. Pettersson, M.; Tuominen, S.; Rasanen, M., IR Spectroscopic Study of H_2O_2, HDO_2, and D_2O_2 Isolated in Ar, Kr, and Xe Matrices. *J. Phys. Chem. A* **1997**, *101*, 1166-1171.
48. Ohno, T.; Masaki, Y.; Hirayama, S.; Matsumura, M., TiO_2-Photocatalyzed Epoxidation of 1-Decene by H_2O_2 under Visible Light. *J. Catal.* **2001**, *204*, 163-168.
49. Liu, Y.; Zhu, Q.; Li, X. Y.; Zhang, G. Z.; Liu, Y. D.; Tang, S. B.; Sharman, E.; Jiang, J.; Luo, Y., Combining High Photocatalytic Activity and Stability Via Subsurface Defects in TiO_2. *J. Phys. Chem. C* **2018**, *122*, 17221-17227.
50. Guan, J. Q.; Duan, Z. Y.; Zhang, F. X.; Kelly, S. D.; Si, R.; Dupuis, M.; Huang, Q. G.; Chen, J. Q.; Tang, C. H.; Li, C., Water Oxidation on a Mononuclear Manganese Heterogeneous Catalyst. *Nat. Catal.* **2018**, *1*, 870-877.
51. Li, Y. F.; Selloni, A., Mechanism and Activity of Water Oxidation on Selected Surfaces of Pure and Fe-Doped NiO_x. *ACS Catal.* **2014**, *4*, 1148-1153.
52. Di Valentin, C.; Tilocca, A.; Selloni, A.; Beck, T. J.; Klust, A.; Batzill, M.; Losovyj, Y.; Diebold, U., Adsorption of Water on Reconstructed Rutile TiO_2(011)-(2×1): TiO Double Bonds and Surface Reactivity. *J. Am. Chem. Soc.* **2005**, *127*, 9895-9903.
53. Modak, B.; Modak, P.; Ghosh, S. K., Efficient Strategy for Enhancement of Visible Light Photocatalytic Activity of $NaTaO_3$ by a Significant Extent. *J. Phys. Chem. C* **2017**, *121*, 12980-12990.
54. Rossmeisl, J.; Qu, Z. W.; Zhu, H.; Kroes, G. J.; Nørskov, J. K., Electrolysis of Water on Oxide Surfaces. *J. Electroanal. Chem*. **2007**, *607*, 83-89.
55. Haschke, S.; Mader, M.; Schlicht, S.; Roberts, A. M.; Angeles-Boza, A. M.; Barth, J. A. C.; Bachmann, J., Direct Oxygen Isotope Effect Identifies the Rate-Determining Step of Electrocatalytic OER at an Oxidic Surface. *Nat. Commun.* **2018**, *9*, 4565.
56. Fierro, S.; Nagel, T.; Baltruschat, H.; Comninellis, C., Investigation of the Oxygen Evolution Reaction on Ti/IrO_2 Electrodes Using Isotope Labelling and On-Line Mass Spectrometry. *Electrochem. Commun.* **2007**, *9*, 1969-1974.
57. Wohlfahrtmehrens, M.; Heitbaum, J., Oxygen Evolution on Ru and RuO_2 Electrodes Studied Using Isotope Labeling and Online Mass-Spectrometry. *J. Electroanal. Chem.* **1987**, *237*, 251-260.
58. Wang, Y. X.; Zhong, W. L.; Wang, C. L.; Zhang, P. L., First-Principles Study of the Electronic Structure of $NaTaO_3$. *Solid State Commun.* **2001**, *120*, 137-140.
59. Zhao, N.; Wang, Y.-H.; Wang, Q.-X.; Hu, W.-J., First-Principles Calculations of the Electronic Structure and Optical Properties of $K_{1-x}Na_xTaO_3$ (X=0, 0.25, 0.5, 0.75, 1). *J. Solid State Chem.* **2012**, *194*, 37-42.
60. Grabowska, E., Selected Perovskite Oxides: Characterization, Preparation and Photocatalytic Properties—a Review. *Appl. Catal. B: Environ.* **2016**, *186*, 97-126.

61. Can, E.; Yildirim, R., Data Mining in Photocatalytic Water Splitting over Perovskites Literature for Higher Hydrogen Production. *Appl. Catal. B: Environ.* **2019**, *242*, 267-283.

Table of Contents

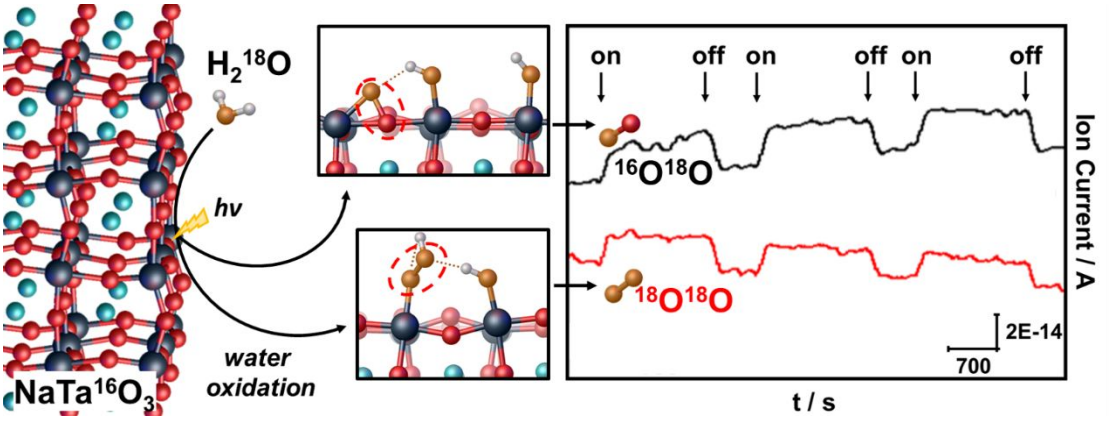

A lattice-oxygen evolved, three-step two-site mechanism is proposed for photocatalytic water oxidation on $NaTaO_3$-based photocatalysts.